Hindawi
Journal of Electrical and Computer Engineering
Volume 2024, Article ID 5556491, 17 pages
https://doi.org/10.1155/2024/5556491

Research Article

An Improved Bi-Switch Flyback Converter with Loss Analysis for Active Cell Balancing of the Lithium-Ion Battery String

Sugumaran G. and Amutha Prabha N.

VIT University, Vellore, India

Correspondence should be addressed to Amutha Prabha N.; amuthaprabha@vit.ac.in

Received 16 August 2023; Revised 27 March 2024; Accepted 17 April 2024; Published 27 April 2024

Academic Editor: Manuela Minetti

This paper focuses on the active cell balancing of lithium-ion battery packs. An improved single-input, multioutput, bi-switch flyback converter was proposed to achieve effective balancing. The proposed topology simplifies the control logic by utilising a single MOSFET switch for energy transfer and two complementary pulses to control the cell-selecting switches. The proposed topology can decrease the number of switching devices as well as the size and cost of the system. The bi-switch flyback converter eliminates the need for a separate buffer circuit to minimise leakage and electromagnetic inductance. Losses and energy efficiency were analysed at each end of the proposed topology. The appropriate MATLAB simulations investigated the balancing characteristics of various state of charge (SOC) imbalances. A comparison is made between the balancing speed and energy transfer efficiency of the proposed topology and a conventional topology that employs a multi-input and multi-output flyback converter in a static mode. The results of the MATLAB simulation were validated by the OPAL-RT (OP5700) real-time simulator. The balancing data of the proposed topology were compared using MATLAB simulation and real-time simulation. This work may reduce the time required to assemble and commission the hardware for the proposed topology's real-time implementation.

1. Introduction

The battery is one of the most promising energy storage devices in recent decades. Lithium-ion batteries can play a vital role in the automobile industry when compared to other batteries such as nickel-based batteries and lead-acid batteries. Lithium-ion batteries can outperform rival batteries with their superior properties, such as high energy density, low self-discharge, long lifespan, lightweight, and no memory effect [1, 2]. For the same reason, lithium-ion batteries are the ideal choice for electric vehicle applications. The historical growth of lithium-ion batteries is described briefly as follows. Lithium-ion battery technologies were introduced in the 1980s and developed in the following decades. The development of lithium-ion batteries mainly depends on the materials used in the battery. The anode, cathode, and electrolyte are the significant components of the battery. The materials used for these components will decide the performance of the battery. In the 1980s, carbon was used as the anode material, lithium cobalt oxide ($LiCoO_2$) was used as the cathode, and lithium hexafluorophosphate ($LiPF_6$) was used as the electrolyte. In the 2000s, graphite was used as the anode material and lithium manganese oxide ($LiMn_2O_4$), lithium-ion phosphate ($LifePO_4$), nickel cobalt manganese (NCM), and nickel cobalt aluminium (NCA) were used as the cathode to increase the energy density of the battery. In this period, gel polymer was used as an electrolyte. In the recent decades, silicon and silicon blends have been used as anode. Lithium-nikel-cobalt-manganese-oxide (Li-Ni-Co-Mn-O) is used as the cathode, and solid-state variants are used as electrolytes. This will increase the battery's energy storage capacity and temperature-withstanding capability [3, 4].

A lithium-ion battery manufacturer can limit the range of current, voltage, and temperature to ensure safe operation. Most commonly, the maximum voltage rating of lithium-ion batteries is in the range of 4.2–4.35 volts per cell. If the voltage exceeds this, it will lead to overcharging, cause

thermal runaway, or reduce battery lifespan. The minimum voltage rating ranges from 2.5 to 2.75 volts per cell; if the cell discharges below this voltage, it will lead to damage, or the battery will be unstable. Hence, a single cell with this voltage rating is insufficient to power an electric vehicle; thus, a battery pack is formed by connecting several cells in series and parallel [5, 6]. The battery pack can be built to meet the voltage and power requirements of EV motors. All cells in the battery pack are not equally charged or discharged due to inconsistencies in battery parameters. This is referred to as cell imbalance. This will cause several adverse effects: cell imbalance reduces battery capacity due to overcharging or overdischarging; finally, it reduces the battery's energy level. Cell imbalance also reduces life span; cells subjected to overcharging or overdischarging may degrade and fail prematurely. Including this, the cell imbalance causes safety risks such as thermal runaway [7, 8]. The effect of cell imbalance is mitigated by using a function called battery management system (BMS). The BMS is crucial for managing and maintaining the performance of the battery. Some significant advantages of BMS are SOC management, state of health (SoH) assessment, balancing, overcurrent and overvoltage protection, temperature management, cell voltage monitoring, fault detection, communication, optimizing charging and discharging, extended battery life, and safety. For cell balancing, the primary function of BMS is to monitor an individual cell's voltage, current, and temperature. BMS can initiate the balancing process to maintain equal charge among all cells. Cell balancing can be accomplished in passive and active methods [9, 10].

The passive cell-balancing method can equalize the voltage or SOC of individual cells in the battery pack. In this technique, the cells with higher voltage or SOC levels can be bypassed or dissipated as heat through passive elements and formulated to lower the charge level to attain a balancing state. Hence, the passive method is also known as the dissipative method [11, 12]. Passive balancing can be achieved by using resistance, bypass diodes, blocking diodes, and passive balancing integrated circuits (ICs). The significant advantages of passive methods are simplicity, reliability, cost-effectiveness, and low maintenance. Compared to the active method, this method is simple and easy to implement. The main drawbacks of this approach are energy loss, heat dissipation, low balancing speed, inefficiency, limited balancing range, and inability to be suitable for all kinds of batteries. In the active cell-balancing method, the equalisation process transfers excessive charge within the cells. Hence, cell balancing is achieved without any energy losses [13, 14]. The common advantages of active cell balancing are fast balancing, high efficiency, precise control, more excellent range, extended battery life, improved safety, optimized energy use, flexibility, remote monitoring and control, and scalability. In active cell balancing, the balancing process can be achieved using inductive charge shuttling, capacitive charge shuttling, transformer charge shuttling, or converter charge shuttling topologies [15, 16]. These methods are most desired for cell balancing to save energy and improve efficiency. The cell-balancing process of the three cells with SOCs of 80%, 30%, and 40% is clearly illustrated in Figure 1. The first part shows the cell imbalance with different SOC levels. The second part shows passive balancing; here, the cells with higher SOCs of 80% and 40% are reduced to those with lower SOCs of 30% to achieve a balancing state. The third part shows the active balancing; here, the cells with different SOC levels can transfer the charge within the cells and attain a balancing state at 50% SOC without any losses.

In capacitive charge shuttling topology, capacitors at various ranges are used to temporally store and transfer energy between cells to attain a balancing state. The capacitive charge shuttling topology has limited usage because it only achieves a balance between adjacent cells; its efficiency decreases as the number of cells increases [17]. The inductive and transformer charge shuttling topologies can transfer energy from any cell to cell in the battery pack to attain a balancing state. Both inductive and transformer charge shuttling topologies use inductors for energy transmission. This topology requires an additional circuit to demagnetise the inducive core, which increases the circuit size and cost [18, 19]. Several studies were conducted to identify a new topology to overcome the abovementioned drawbacks.

However, the converter-based charge shuttling topology has numerous advantages, such as high balancing accuracy, compact size, high balancing speed, and low cost. Also, the converter-based charge shuttling topology can transfer energy using cell-to-cell, cell-to-pack, and pack-to-cell techniques [20, 21]. Due to the abovementioned advantages, the converter-based balancing topology can lead to all other balancing topologies. Converters such as buck-boost, Cuk, resonant, ramp, push-pull, dual active bridge, and flyback converters participate in a converter-based cell balancing. After thoroughly examining the various literature, the flyback converter has more advantages than others [22, 23]. The positive aspects of a flyback converter are the electrical isolation between the input and output sides, the ability to supply multiple output voltages, high-speed balancing, reduced heat generation, optimized energy use, compatibility with various battery chemistries, remote monitoring and control, and the reduced number of switching devices [24, 25]. From the abovementioned benefits, one can conclude that the flyback converter is the most desired candidate for cell balancing. Even though some flaws in previous literature on flyback converters are noticed, such as losses due to the iron core, copper winding, and leakage inductance, the cost may increase as the number of windings increases [26, 27]. The flaws mentioned on flyback converter-based cell balancing are considered and minimised with the proposed topology.

This paper concentrates on improving balancing speed and energy transfer efficiency with a proposed active cell-balancing system using a bi-switch flyback converter. The balancing process was implemented for the six-series and one parallel (6S1P) lithium-ion battery pack. The Coulomb counting method is used for SOC estimation for the proposed topology. The proposed topology can be designed, and their results are verified by MATLAB tools and a real-time OPAL-RT (OP5700) simulator. This paper is organised as follows. Following the introduction of the properties of the bi-switch flyback converter, the converter design, SOC estimation, and

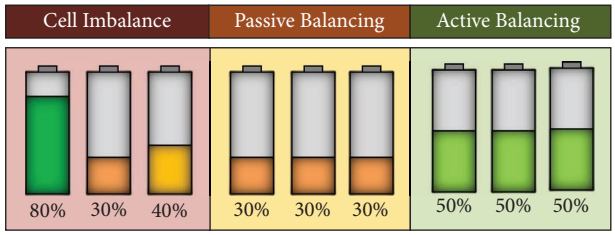

Figure 1: Balancing topology.

step-by-step balancing process are explained in Section 2. Section 3 describes the balancing principle and loss analysis. Section 4 elaborates on the simulation result with different imbalances, such as some high and some low SOC imbalances, some high and some low SOC imbalances, and some low and some high SOC imbalances. The simulation result was verified with the real-time simulator in Section 5. Finally, this paper ends with a conclusion in Section 6.

2. Proposed Topology

2.1. Structure of the Balancing Circuit. The proposed architecture in this study consists of a modified bi-switch flyback converter for energy transformation to achieve a balancing condition. Figure 2 depicts the structure of the proposed topology. The balancing circuit is designed for a six-series and one parallel lithium-ion battery pack (6S1P) configuration. The critical flaws in the prior study were discovered, and the proposed topology was designed to address the existing problems. Some current challenges and their resolution in the proposed topology were discussed. The balancing circuit [28] consists of the multi-input and multioutput flyback converter. For energy transformation, each cell is connected to its own flyback transformer. This leads to more complex designs and higher costs. The switch on either side of the flyback transformer is turned on simultaneously for balance purposes. Balancing operations requires a large number of power switches, intricate driving circuits, and complex controllers. The proposed topology in this work combines a modified bi-switch flyback converter with a single-input, multioutput flyback converter. It decreases the amount of copper windings, lowering both the initial cost and the copper loss. It also minimises circuit complexity.

The cell-balancing control circuit [29] employs a single input and selective output (SISO) bi-switch flyback converter. The circuit is designed to allow the cells to pack and shift energy from cell to cell in order to achieve a balancing condition. To transform energy, the two switches on the primary side of the flyback transformer are triggered at the same time. It has been discovered that only one switch needs to be activated simultaneously to transfer energy rather than two. Furthermore, more inductors are employed on the secondary side of the transformer, increasing leakage inductance and losses. In this proposed topology, just one switch is activated at a time on the primary side of the flyback transformer rather than two. As a result, the number of switching activities is minimised in order to minimise

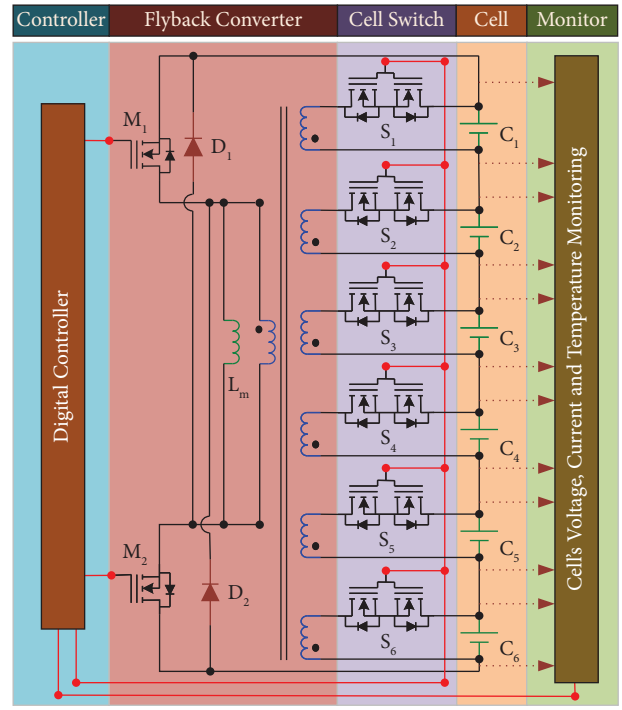

Figure 2: Structure of the proposed balancing circuit.

switching losses. The suggested architecture uses energy transformation strategies from cell to pack and pack to cell.

The bi-switch flyback converter in [30] can alleviate voltage stress on the power switches. However, the topology needs four switches for each energy conversion, necessitating a sophisticated controller. A double passive snubber circuit is also used to prevent the high voltage spikes caused by the leakage inductance. The resonant bi-switch flyback converter in [31] is designed for power factor adjustment by connecting a capacitor and an inductor in series with the transformer's secondary winding. The zero current switch is achieved using resonance for switches and diodes; however, the circuit operates in discontinuous conduction mode, resulting in higher current stress and power switches. The bi-switch flyback converter in the proposed topology of this study utilises only two switches for each energy conversion, and two free-wheeling diodes can feed back the reverse power of leakage inductance to the source; hence, voltage spikes are reduced without any snubber circuit, which reduces the losses and increases the balancing efficiency. Figure 3 shows the balancing circuit of the existing topology [28] for reference. It consists of a separate flyback transformer for each cell. Individual switches connected on both sides of the flyback transformer can control the energy transfer among each cell. A programmable controller will control each switch. For simplicity, the snubber circuit and filter circuits are hidden in the conventional topology.

2.2. Converter Design. The converter design includes two modes of operation. In the first mode, a MOSFET switch is in an ON state; and the primary inductor voltage V_{Lp} is given by

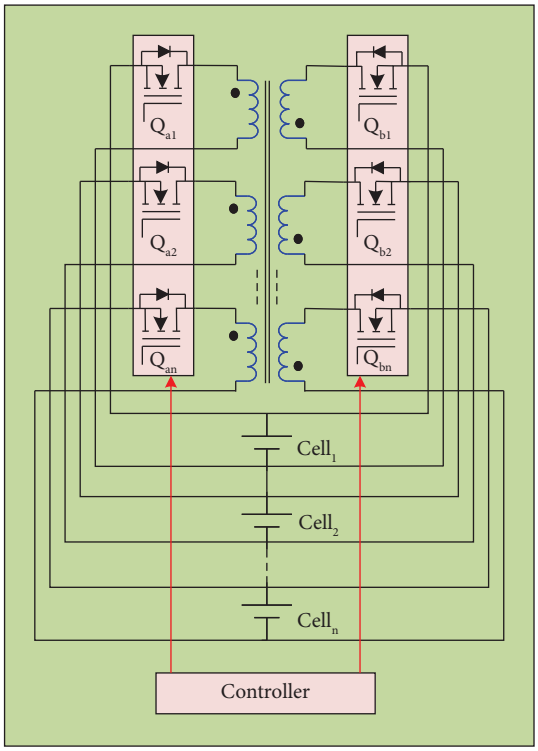

Figure 3: Conventional balancing circuit.

$$V_{\mathrm{Lp}} = V_{\mathrm{Battery}}. \tag{1}$$

The ON time T_{on} of the switching device is calculated as

$$T_{\mathrm{on}} = \mathrm{DT}_t, \tag{2}$$

where D is the duty cycle and T_t is the total period.

The primary inductor current I_{Lp} is calculated as

$$I_{\mathrm{Lp}} = \frac{V_{\mathrm{Battery}}}{L} \times T_{\mathrm{on}}. \tag{3}$$

In the second mode, a MOSFET switch is in an OFF state, and the primary inductor voltage is given by

$$V_{\mathrm{Lp}} = \frac{-V_{\mathrm{Cell1}}}{n} + \frac{-V_{\mathrm{Cell2}}}{n} + \ldots\ldots + \frac{-V_{\mathrm{Cell}m}}{n}, \tag{4}$$

where $m = 1, 2, 3, \ldots, 6$ is the number of cells and n is the duty ratio.

The OFF time of the switching device is estimated as

$$T_{\mathrm{off}} = (1 - D) \times T_t. \tag{5}$$

The primary inductor current during MOSFET in the OFF state is considered as zero.

$$I_{\mathrm{Lp}} = 0. \tag{6}$$

The average voltage across the inductor during steady-state conditions is given as

$$T_{\mathrm{on}} \times V_{\mathrm{Lp}} = V_{\mathrm{Battery}} \times D \times T_t \,(\text{during MOSFET in ON state}), \tag{7}$$

$$T_{\mathrm{off}} \times V_{\mathrm{Lp}} = \frac{V_{\mathrm{Cell},m}}{n} (1 - D) \times T_t \,(\text{during MOSFET in OFF state}). \tag{8}$$

For simplicity, we assume only one secondary winding when calculating the primary current. We take the battery output voltage as 3.6 V and assume a 2 A output current. The output power is calculated as

$$P_{\mathrm{out}} = V_{\mathrm{out}} \times I_{\mathrm{out}} = 7.2W. \tag{9}$$

The efficiency will be considered 100% for an ideal diode and switch, which means that $P_{\mathrm{in}} = P_{\mathrm{out}}$. The average primary current $I_{P,\mathrm{ave}}$ can be expressed as

$$I_{P,\mathrm{ave}} = \frac{P_{\mathrm{in}}}{V_{\mathrm{Battery}}}, \tag{10}$$

$$V_{\mathrm{Battery}} = n \times c \frac{D}{(1 - D)} \times V_{\mathrm{Cell},m} = 21.6V, \tag{11}$$

$$I_{P,\mathrm{ave}} = 0.33A. \tag{12}$$

The average primary peak current $I_{\mathrm{pp,ave}}$ is given by

$$I_{\mathrm{pp,ave}} = \frac{1}{T_p} \int_0^{T_p} I(t)\mathrm{d}t = \frac{(1/2) \times I_{\mathrm{Peak}} \times D \times T_p}{T_p} = 0.5 \times I_{\mathrm{Peak}} \times D, \tag{13}$$

$$I_{\mathrm{Peak}} = \frac{I_{P,\mathrm{ave}}}{0.5 \times D} = 1.32A. \tag{14}$$

The primary inductance can be calculated as

$$V = L\frac{\mathrm{d}i}{\mathrm{d}t}, \tag{15}$$

$$L_p = \frac{V}{\mathrm{d}i} \times \mathrm{d}t, \tag{16}$$

$$L_p = \frac{V_{\mathrm{Battery}}}{I_{\mathrm{Peak}}} \times T_{\mathrm{on}}, \tag{17}$$

where ON time T_{on} is derived from D/f_{sw}.

$$L_p = \frac{21.6}{1.32} \times 10\mu s = 163.6\mu H. \quad (18)$$

For calculating magnetising inductance (L_m), we assume that the flyback converter has an efficiency of 85%. In the proposed system, six cells are connected in series with a voltage range of 3.6 V each, so the minimum input voltage is 21.6 V, the duty cycle D is 0.5, and the switching frequency is 50 kHz.

The magnetising inductance is given by

$$L_m = \frac{\left(\eta \times V_{\text{in,min}} \times D\right)^2}{2 \times P_{\text{in}} \times f_{\text{sw}}} = 117\mu H. \quad (19)$$

2.3. SOC Estimation. The SOC is one of the critical parameters of a battery. SOC is the state of charge (SOC), defined as the ratio of available battery capacity $Q(t)$ to nominal capacity Qn of the battery [32, 33]. The SOC at a particular time (SOC(t)) is given by

$$\text{SOC}(t) = \frac{Q(t)}{Qn}. \quad (20)$$

The SOC cannot be directly measured but can be estimated by using any open circuit voltage method, Coulomb counting (CC) method, Kalman filter (KF) method, or a hybrid method. The Coulomb counting method, also known as the ampere counting method or current integrating method, is the most commonly used technique for real-time applications. This method will not focus on the battery's internal characteristics and structure [34, 35]. This paper estimates SOC by using the Coulomb counting method. The mathematical expression for estimating SOC using the Coulomb counting method is as follows:

$$\text{SOC}(t) = \text{SOC}(0) - \frac{\eta}{Q}\int_0^t I\,dt, \quad (21)$$

where SOC(t) is an estimated SOC at a time "t," SOC(0) is the initial SOC or SOC at time $t = 0$, η is the coulombic efficiency, Q is the rated capacity, and "I" is the discharging current. We assume that coulombic efficiency is unity and $Q = 3600^*$ Ah.

2.4. Step-by-Step Balancing Process. Figure 4 depicts the sequential process of active cell balancing based on the proposed bi-switch flyback converter. To initiate the balancing procedure, the initial SOC value of each cell is arbitrarily determined. The battery pack in this paper consists of six cells connected in series. Each cell's initial SOC will be 78%, 72%, 77%, 71%, 76%, and 70%, respectively. The following step will calculate the mean SOC value across all cells. Then, each cell's SOC will be compared to the average SOC value, and the cell with the most significant deviation will be identified. Then, the modes of operation are selected; if a cell's SOC value is below the average SOC value, then the boost mode of operation is selected. Therefore, the battery pack's energy is transferred to the selected cell to achieve a balanced state. If the selected cell's SOC is greater than the average SOC, the buck mode of operation is selected. After the buck operating mode, energy is transferred from the selected cell to the battery pack to achieve a balanced state. This procedure was repeated for each cell until their SOC values were identical. The balancing process is completed when all the cells reach the same SOC value.

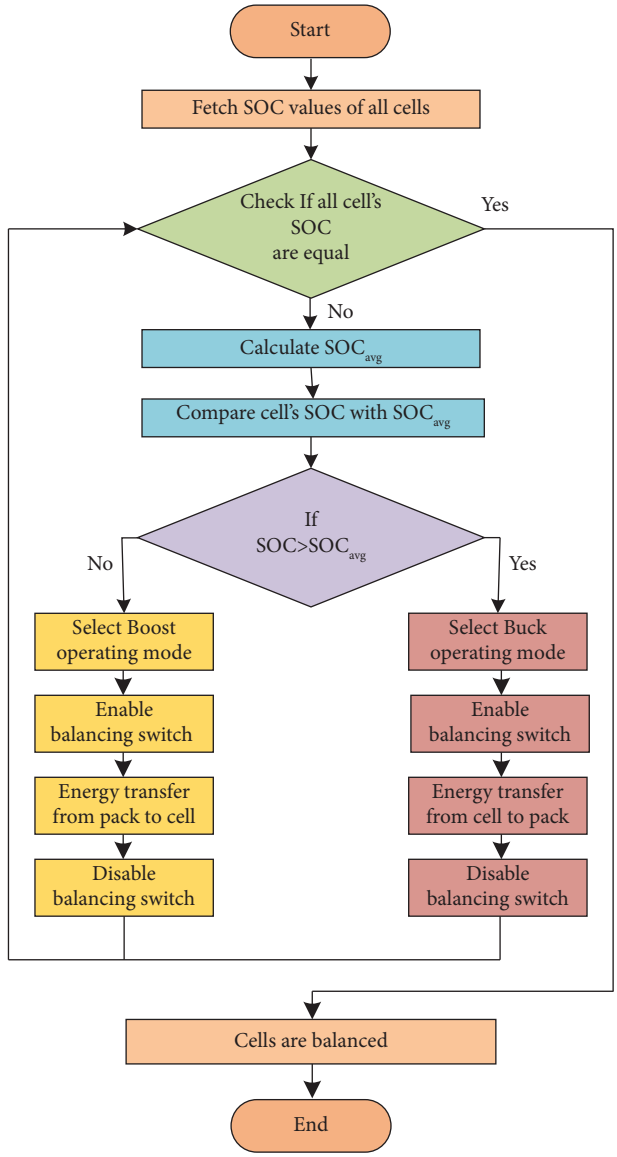

Figure 4: Balancing flowchart.

3. Balancing Principle and Loss Analysis

3.1. Balancing Principle. This paper used a bi-switch flyback converter with a single input and multiple output windings for cell balancing. The flyback converter is designed to operate in discontinuous conduction mode (DCM). Consequently, the stored energy in the transformer's inductance is discharged during each switching cycle. In each switching cycle, the magnetic flux must be restored to its actual size; as a result, electromagnetic interference is reduced with each

cycle. Since the flyback converter operates in discontinuous conduction mode, it can avoid core saturation and increase the energy utilisation rate.

To illustrate the balancing principle, we assume that cell 6 has a lower SOC than that of the other cells. This condition is detected by a conventional SOC estimation method called the Coulomb counting method. The SOC-based balancing algorithm is loaded in the controller, and boost mode will be activated, which can transfer energy from the battery pack to cell 6 to achieve an equilibrium state by activating corresponding switches. To simplify the balancing procedure, the parasitic parameters of the balancing circuit were disregarded, and the switching cycle maintained a constant terminal voltage. Either boost or buck operation was used to accomplish the balancing process. Boost operation denotes transferring energy from the battery pack to the cell, and buck operation denotes transferring energy from the cell to the battery pack.

Figure 5 depicts the balancing procedure between the battery pack and cell 6. Each cell is connected to the secondary winding of the flyback transformer. The primary and secondary circuits are alternately activated to achieve a balanced state by either buck operation or boost operation. Two modes comprise the work process. The primary winding is connected to the battery pack during the first mode because switch M_1 is turned on. The transformer's primary inductance can store energy with a positive charge on the upper side and a negative charge on the lower side. The current from the battery pack I_b will flow through M_1, inductance, and the body diode of M_2; the body diode of switch M_1 will also prevent the reverse current. The first mode of the work process is depicted in Figure 5(a). During the second mode of operation, switch M_1 is deactivated, and switch S_6 is activated. The electromotive force induced in the secondary winding is positive on the upper side and negative on the lower side. Polarity was altered due to magnetic coupling. Consequently, energy can be transferred from the secondary winding to cell 6, which is boosted to achieve a balanced state. Simultaneously, the energy stored in the leakage inductance L_m can feed back to the battery pack via D_1 and D_2 with reverse polarities, such as negative on the upper side and positive on the lower side of the leakage inductance. The second mode of work progress is depicted in Figure 5(b). For the buck operation, the abovementioned process was reversed. Hence, energy can transfer from the cell to the battery pack to achieve a balancing state. The excess energy in cell 6 is stored in the secondary side inductance through switch S_6, and the induced energy in the primary side inductance is transferred to the battery pack through switch M_2 and the body diode of switch M_1.

3.2. Loss Analysis. The losses of each component in the balancing circuit were estimated for the best performance of the balancing process. The total losses include losses due to switching devices and flyback transformers. Switching and conduction losses are losses that come under the switching devices. The ohmic loss and core loss are losses due to the flyback transformer. Let us consider the following notations for loss analysis: R_{sp} is the primary switch resistance of MOSFET M_1, R_{ss} is the secondary switch resistance of MOSFET S_6, L_m is the magnetising inductance of the transformer, V_{gp} is the primary gate voltage of MOSFET M_1, V_{gs} is the secondary gate voltage of MOSFET S_6, V_{tp} is the primary terminal voltage of MOSFET M_1, V_{ts} is the secondary terminal voltage of switch S_6, "i_L" is the primary inductance current, and "i_D" is the secondary switch current [28, 36].

Let us consider the boost mode of operation for loss analysis. Figures 6(a) and 6(b) show the equivalent circuit of mode 1 and mode 2 of boost operation. The ideal source voltage is represented as V_p, and the cell voltage is represented as V_c.

Determining accurate switching losses is very complex. Hence, the loss estimation process of MOSFET [37] is considered. The switching loss P_{sw} can be calculated as follows:

$$P_{\mathrm{sw}} = \frac{1}{2} I_{\mathrm{sw}} V_{\mathrm{tp}} t_{\mathrm{sw}} f_{\mathrm{sw}} + \frac{1}{2} C_p V_{\mathrm{tp}}^2 f_{\mathrm{sw}}, \tag{22}$$

where I_{sw} is the switching current of MOSFET M_1, t_{sw} is the switching period ($t_{\mathrm{on}} + t_{\mathrm{off}}$), f_{sw} is the switching frequency, C_p is the parasitic capacitance of MOSFET, and V_{tp} is the primary terminal voltage of MOSFET M_1.

After switching loss, conduction loss can be analysed during energy transfer through the flyback transformer. Considering the boost operation for calculating conduction loss, the boost operation can be obtained in two modes illustrated in Figure 5, and the switching waveform of the boost operation is shown in Figure 7. During the first switching period (t_0–t_1), the MOSFET switch M_1 is turned on. The battery pack voltage V_p was stored in the transformer's primary inductance L_m since the current i_L was increased linearly through wire resistance (R_w) and the primary switch resistance of MOSFET M_1 (R_{sp}) [37, 38]. The losses on the primary side of the flyback transformer are given in the following equations, where W_{R_w} is the loss due to wire resistance and $W_{R_{\mathrm{sp}}}$ is the loss due to the primary switch resistance of MOSFET M_1.

$$W_{R_w} = i_L^2 R_w (t - t_0), \tag{23}$$

$$W_{R_{\mathrm{sp}}} = i_L^2 R_{sp} (t - t_0). \tag{24}$$

At the end of the first switching period, $t = t_1$, MOSFET M_1 is turned off. During the second switching period (t_1–t_2), the MOSFET switch S_6 is turned on. Cell 6 will be charged by the energy stored in the magnetizing inductance L_m through current i_D. During this switching period, the current i_D will decrease linearly. The loss due to the secondary switch resistance $W_{R_{\mathrm{ss}}}$ of MOSFET switch S_6 is given as follows:

$$W_{R_{\mathrm{ss}}} = \left(\frac{i_D}{N}\right)^2 R_{\mathrm{ss}} (t - t_1). \tag{25}$$

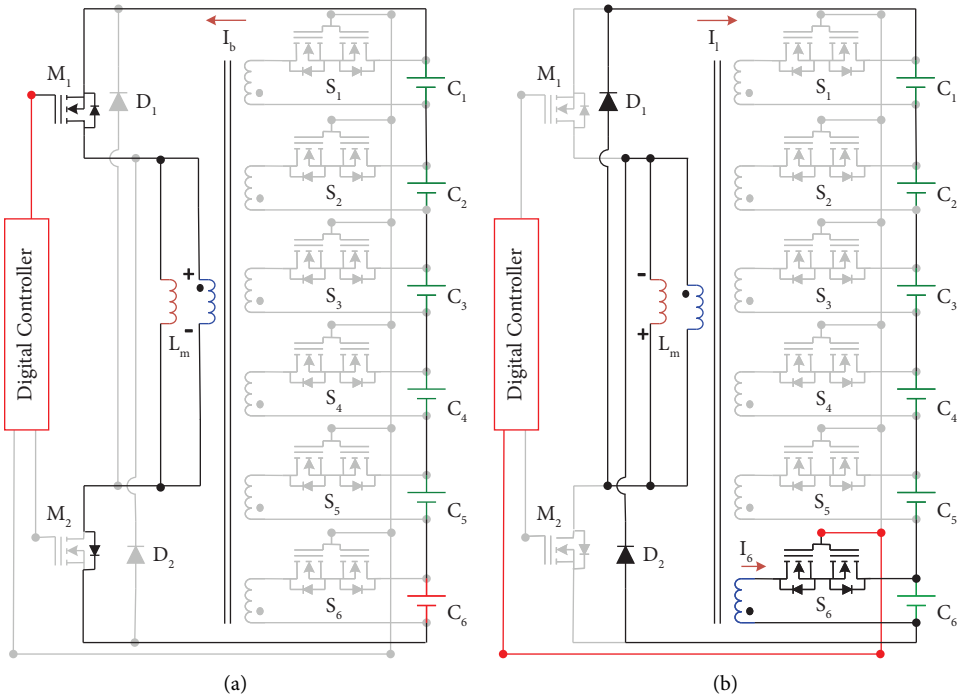

Figure 5: Cell balancing principle among battery pack and cell 6. (a) Mode 1. (b) Mode 2.

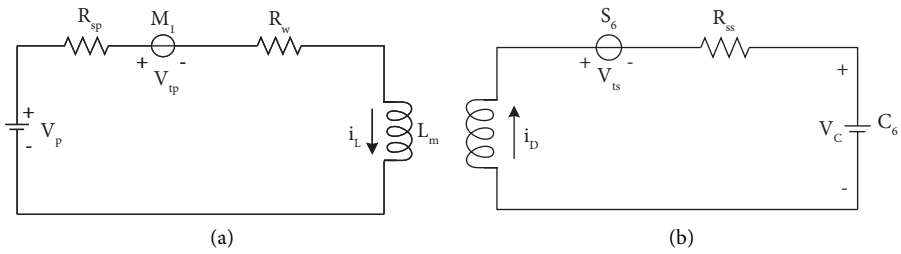

Figure 6: Equivalent circuit. (a) Mode 1. (b) Mode 2.

The conduction loss during the switching period is calculated by using losses on the primary side and secondary side of the transformer ($P_{R_{sp}}, P_{R_{ss}}$), and the duty ratio is given by the following equations:

$$D = \frac{(t_1 - t_0)}{t_{sw}}, \tag{26}$$

$$1 - D = \frac{(t_2 - t_1)}{t_{sw}}. \tag{27}$$

Generally, the conduction loss mainly depends on switch resistance R_s, current i_L, and duty ratio D. The conduction loss P_{con} is given as

$$P_{con} = P_{R_{sp}} + P_{R_{ss}}, \tag{28}$$

$$P_{R_{sp}} = \frac{W_{R_{sp}}}{t_{sw}} = i_L^2 R_{ps} D, \tag{29}$$

$$P_{R_{ss}} = \frac{W_{R_{ss}}}{t_{sw}} = \left(\frac{i_D}{N}\right)^2 R_{ss}(D - 1). \tag{30}$$

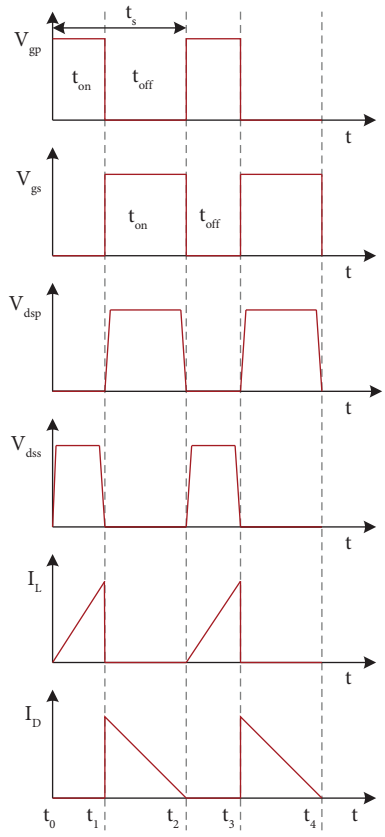

Figure 7: Switching waveform.

The losses due to the flyback transformer include ohmic loss (P_{ohmic}) and core loss (P_{core}). The ohmic loss can occur in the transformer's primary and secondary winding. The ohmic loss is given by

$$P_{\text{ohmic}} = i_L^2 R_{\text{sp}} + i_D^2 R_{\text{ss}}, \tag{31}$$

where i_L and i_D are the transformer's primary current and secondary current and R_{sp} and R_{ss} are the primary switching resistance and secondary switching resistance.

The core loss includes eddy current loss and hysteresis loss. The eddy current loss (P_e) is calculated using the maximum flux density (B_m), frequency (f), lamination thickness (t), and eddy current constant (η_e).

$$P_e = \eta_e B_{\max}^2 f^2 t^2. \tag{32}$$

The hysteresis losses (P_h) can be calculated by using the maximum flux density (B_m), frequency (f), core volume (V), and eddy current constant (η_h).

$$P_h = \eta_h B_{\max}^{1.6} f V, \tag{33}$$

$$P_{core} = P_e + P_h. \tag{34}$$

The real-time core loss calculation is complicated because the relevant transformer parameters, such as transformer material, temperature, flux density, and excitation current, are complex to collect from the manufacturer. Hence, to simplify the core loss calculation, this paper uses the material PC40 for collecting the transformer parameters.

$$P_{\text{core}} = 1.31210^{-6} f^{1.404} \left(\frac{\Delta B}{2}\right)^{2.286} V, \tag{35}$$

where ΔB is the variation of the transformer's magnetic intensity and V is the volume of the transformer core. The total losses for the system's first switching period can be calculated as cumulative switching loss, conduction loss, ohmic loss, and core loss.

$$P_{\text{total}} = P_{\text{sw}} + P_{\text{con}} + P_{\text{ohmic}} + P_{\text{core}}. \tag{36}$$

The loss analysis of the boost mode of operation is discussed in the abovementioned description, and the same procedure will be followed for the buck mode of operation. The current direction is changed in the buck mode, which is the only difference compared to the boost mode of operation. Hence, this paper does not concentrate on the loss analysis of buck mode operation. For the proposed topology, the input power is 23.4 Wh, the total power loss is calculated as 2.3691 W, and the energy efficiency of the proposed topology is calculated by using the following equation:

$$\eta_{\text{energy}} = 1 - \frac{p_{\text{total}}}{P_{\text{in}}} \times 100\%, \tag{37}$$

where η_{energy} is the energy efficiency, p_{total} is the total power loss, and P_{in} is the input power.

4. Simulation Result

Using MATLAB simulation software, the proposed system's performance was verified and analysed. Consequently, a six-cell series and one-cell parallel (6S1P) battery pack with a voltage rating of 22 V and a capacity of 6.5 Ah was designed. This paper focuses primarily on analysing the performance of static balancing through simulation experiments. The performance of the proposed topology is compared with the conventional topology [28]. The simulation parameters of the proposed topology are given in Table 1, which is based on the parameters of conventional topology. Figure 8 illustrates the simulation circuit of the proposed topology. The proposed circuit is intended for a 6S1P battery pack. It consists of a bi-switch flyback transformer with a single input and multiple outputs, selecting switches, a controller, and a monitor. The schematic of conventional topology is depicted in Figure 3. The circuits of the proposed and conventional topologies set the same initial SOC value; therefore, the performance of both topologies was analysed. Three categories of static analysis were performed on the proposed topology. In the first category, some highest and some lowest SOC imbalances were considered; in the second category, one highest and some lowest SOC imbalances were considered; and in the third category, one lowest SOC imbalance and some highest SOC imbalances were considered.

4.1. Category 1. The initial SOC of cells in this category is fixed, as shown in Table 2. Cells 1, 3, and 5 are fixed to higher-than-average SOC values, whereas cells 2, 4, and 6 are fixed to lower-than-average SOC values; thus, they are categorised as some high and some low SOC imbalances. Figure 9 depicts the simulation results for this instance's proposed and conventional topologies. The conventional topology was balanced in 2523 seconds, while the proposed topology required 1210.5 seconds to achieve equilibrium.

4.2. Category 2. The initial SOC of cells is fixed in this category, as shown in Table 3. Cell 1 is fixed to a higher-than-average SOC value, whereas cells 2, 3, 4, 5, and 6 are fixed to lower-than-average SOC values; consequently, they are classified as one high and some low SOC imbalances. Figure 10 depicts the simulation results for this instance's conventional and proposed topologies. The conventional topology was balanced at 1550 seconds, while the proposed method was balanced at 1460 seconds.

4.3. Category 3. The initial SOC of cells is fixed in this category, as shown in Table 4. Cells 1, 2, 3, 4, and 5 are fixed to SOC values of higher than average, whereas cell 6 is fixed to SOC values of lower than average; therefore, it is classified as some high and one low imbalance. In this instance, Figure 11 depicts the simulation results for the conventional topology and the proposed topology. The conventional topology was balanced at 1710 seconds, while the proposed topology took 1520 seconds.

Table 1: Simulation parameters of the proposed topology.

Parameters	Value	Description
Nominal cell voltage	3.6	Volt
Rated cell capacity	6.5	Ah
Fully charged voltage	4.2	Volt
Transformer turns ratio	1 : 1	Np/Ns
Primary inductance	163.6	μH
Secondary inductance	163.6	μH
Switching frequency	50	kHz
Duty cycle	50	%

The SOC value of the starting and ending of the balancing processes was used to analyse energy efficiency for different imbalances. The energy efficiency can be calculated as

$$\eta_{b\,(\mathrm{MATLABsimulation})} = \frac{n\mathrm{SOC}_e}{\sum_{i=1}^{n}\mathrm{SOC}_s}, \tag{38}$$

where $\eta_{b(\mathrm{MATLABsimulation})}$ is the MATLAB simulation balancing efficiency, n is the number of cells, $\mathrm{SOC_e}$ is the state of charge at the end of the balancing process, and $\mathrm{SOC_S}$ is the state of charge at the starting of the balancing process. The balancing efficiencies of the conventional topology for the three categories are 98.3%, 98.4%, and 96.1%, whereas for the proposed topology, 98.78%, 99%, and 96.8% are observed. A comparison of the balancing efficiency and balancing speed of the proposed topology and conventional topology is shown in Figures 12 and 13. Figure 12 clearly shows that the balancing efficiency of the proposed topology is 0.4%–0.7% higher than that of the conventional topology. Figure 13 demonstrates that the balancing speed of the proposed topology is faster than the conventional topology.

5. Real-Time Simulator Implementation

The bi-switch flyback converter-based active cell-balancing topology was evaluated using the OPAL-RT (OP5700) hardware in the loop (HIL) simulator. The primary objective of a real-time simulator is to reduce cost, time, and risk and identify workable solutions for electrical drives, grids, power systems, automobiles, and aerospace applications. The setup for the OP5700 real-time simulator is depicted in Figure 14. On the host computer, RT-LAB simulation software was installed. Using a local area network (LAN), the host PC was connected to the real-time simulator. The configuration of the real-time simulator is operable in four modes: edit, build, load, and execute. In the edit mode, the simulation circuit is edited by the requirements of the RT-LAB software. Also, the number of analogue output ports, type of solver, sampling time, and communication channels are selected. In the build mode, the C-code for the simulation model was generated, and a real-time simulator was integrated. Then, the real-time simulator is prepared to synchronise with the RT-LAB software model so that it can be executed. In the execution mode, hardware synchronisation will be chosen, allowing the simulator to provide real-time outputs via an analogue output port.

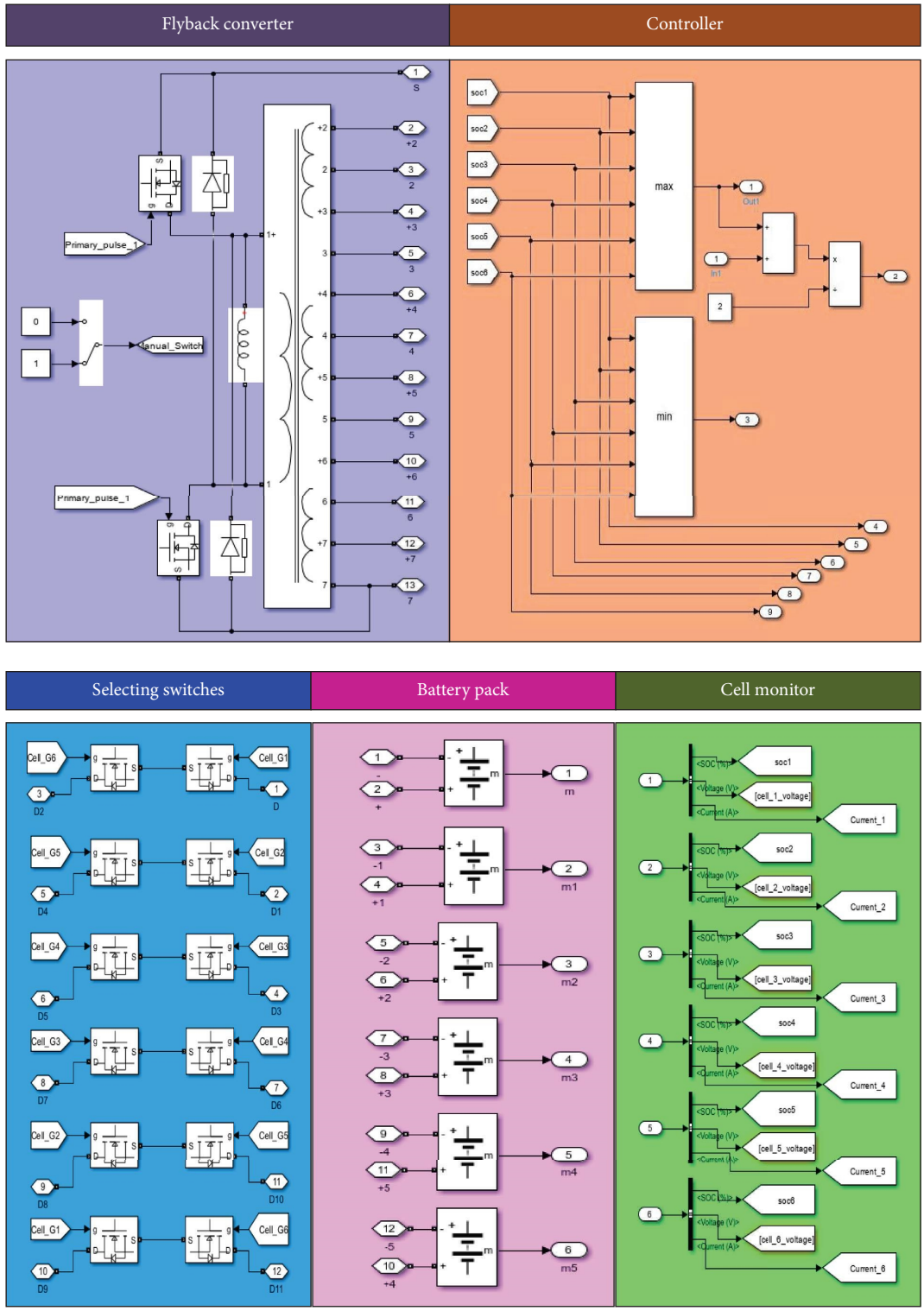

Figure 8: Simulation circuit of the proposed topology.

Table 2: Initial SOC of some high and some low imbalances.

Cell	Cell 1 (%)	Cell 2 (%)	Cell 3 (%)	Cell 4 (%)	Cell 5 (%)	Cell 6 (%)
State of charge	78	72	77	71	76	70

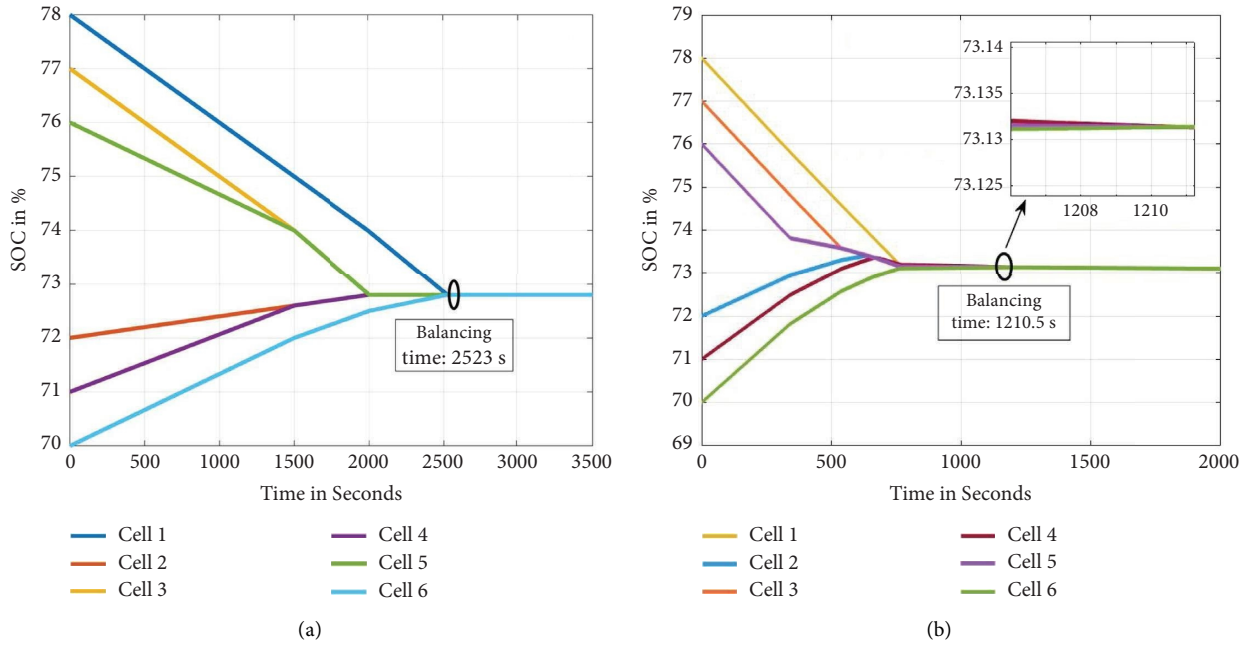

Figure 9: Simulation output of some high and some low imbalances. (a) Conventional topology. (b) Proposed topology.

Table 3: Initial SOC of one high and some low imbalances.

Cell	Cell 1 (%)	Cell 2 (%)	Cell 3 (%)	Cell 4 (%)	Cell 5 (%)	Cell 6 (%)
State of charge	78	72	74	71	73	70

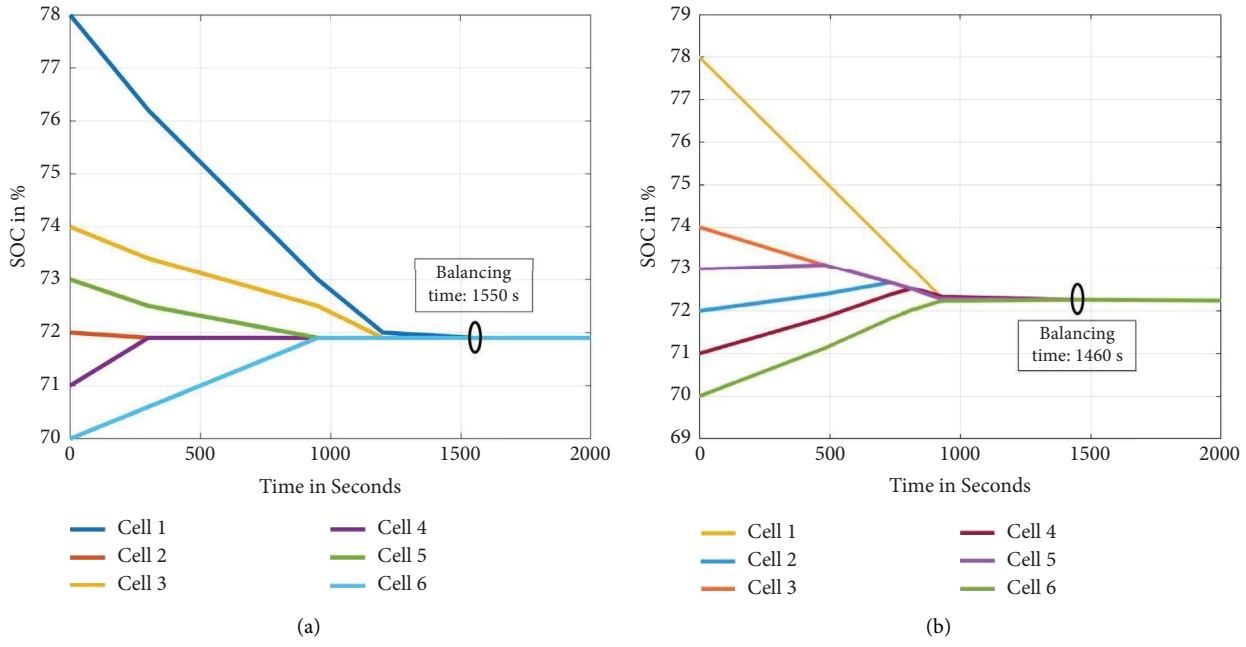

Figure 10: Simulation output of one high and some low imbalances. (a) Conventional topology. (b) Proposed topology.

Table 4: Initial SOC of some high and one low imbalances.

Cell	Cell 1 (%)	Cell 2 (%)	Cell 3 (%)	Cell 4 (%)	Cell 5 (%)	Cell 6 (%)
State of charge	78	75	77	74	76	70

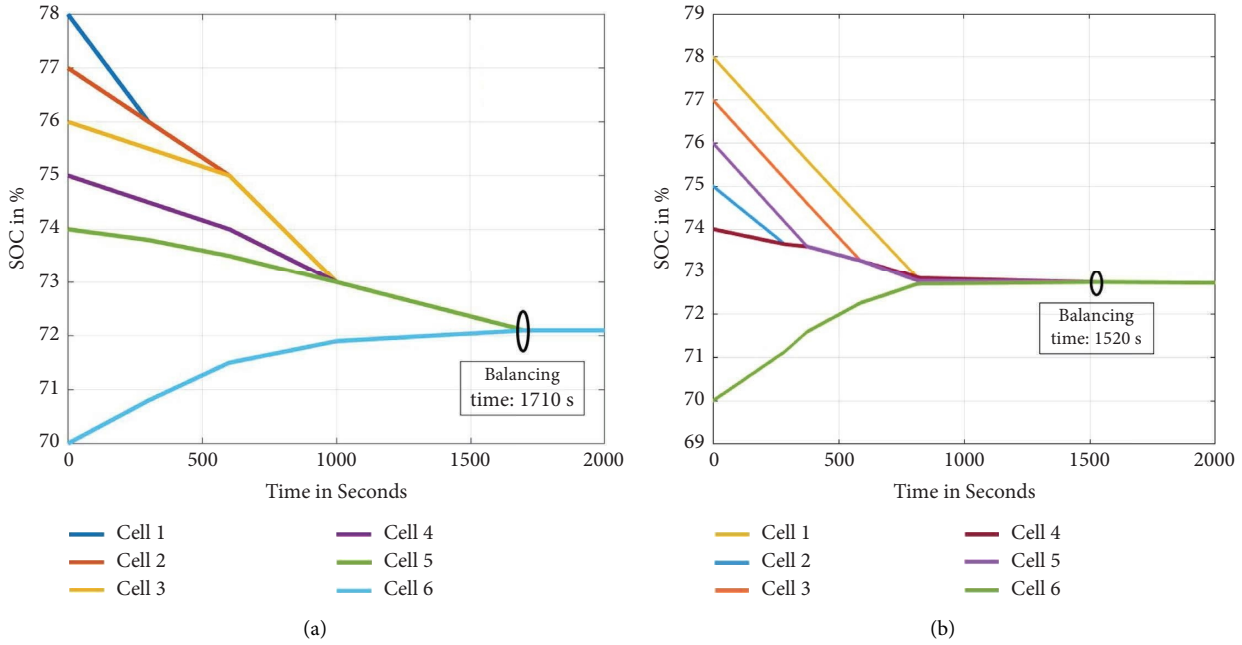

Figure 11: Simulation output of one low and some high imbalances. (a) Conventional topology. (b) Proposed topology.

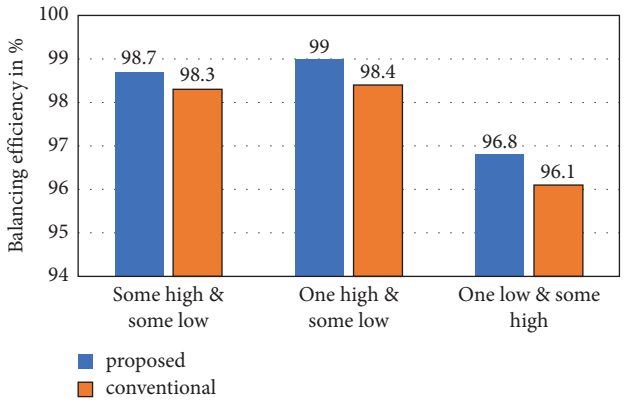

Figure 12: The energy efficiency of proposed and conventional topologies.

Table 5 lists the OPAL-RT (OP5700) real-time simulator's specifications [39, 40].

5.1. Real-Time Simulation Result. The proposed topology's output was validated using the OPAL-RT (OP5700) Real-time HIL simulator. The DSO's channels limit the number of outputs in the OP5700 simulator. In this paper, the simulator output can be validated using a two-channel DSO, allowing simultaneous analysis of the two cells' balancing parameters. Initially, cells 1 and 2 can be validated. The HIL simulator can be executed after selecting a fixed-type solver, two analogue output ports, a 5 ms sampling time, and an infinite stop time. Figure 15 demonstrates the output of the real-time simulator. The some high and some low SOC imbalance (static) mode properties of MATLAB simulation were considered for real-time validation. The balancing processes began at 78% SOC in cell 1 and 72% SOC in cell 2 based on the initial SOC values of cells 1 and 2. The SOC of cell 1 and cell 2 before balancing is depicted in Figure 15(a), while the SOC of the same cells after balancing is depicted in Figure 15(b). Therefore, cells 1 and 2 achieve equilibrium at SOC of 73.5% and 73%, respectively. The prediction of exact balancing time in a real-time simulator is extremely challenging due to the infinite stop time in a real-time simulator.

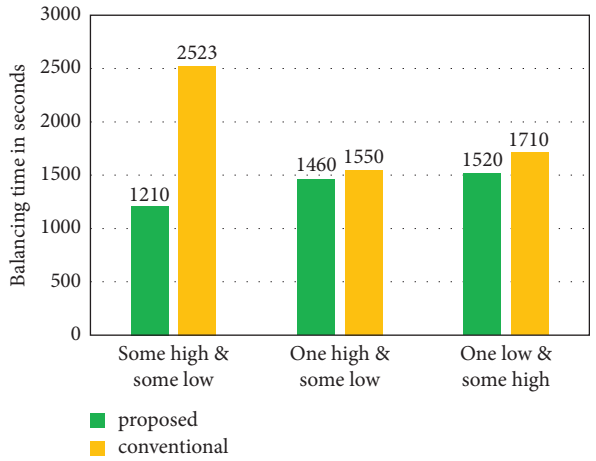

Figure 13: Balancing speed of proposed and conventional topologies.

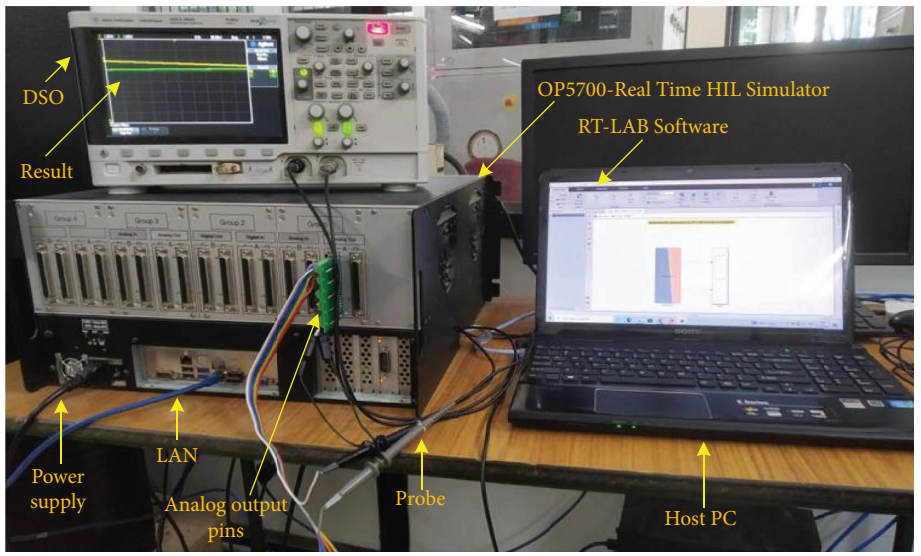

Figure 14: OPAL-RT (OP5700) real-time simulator setup.

Table 5: Real-time simulator specification.

Name	Specification
Product	OP5700
Nominal capacity	100–240 V AC, 50–60 Hz, 8 A-4 A, 600 W
FPGA (field-programmable gate array)	Xilinx Virtex-7 FPGA on VC707 board
Hard disk	512 GB SSD
Input/output lines	256 lines, 8 analog or digital, 16 or 32 channels
Communication port	16SFP socket, up to 5 Gbps
Input/output connectors	4 panels of 4DB37F connectors
PC interface	Standard PC interface
Monitoring connectors	4 panels of RJ47 connectors

Following the preceding result, the balancing parameters of cells 3 and 4 are examined. Figure 16 depicts the outcome of the real-time simulation. 77% and 71% SOC can be used to initiate the balancing processes of cell 3 and cell 4, respectively. Figures 16(a) and 16(b) depict the SOC of cells before and after balancing. From the result, it is observed that cell 3 is balanced at SOC of 72.5% and cell 4 is balanced at SOC of 72%.

Finally, the balancing parameters for cells 5 and 6 were analysed, and their real-time simulator results are depicted in Figure 17. These cells begin balancing processes between 76% and 70% of SOC. Figure 17(a) depicts the SOC of cells 5

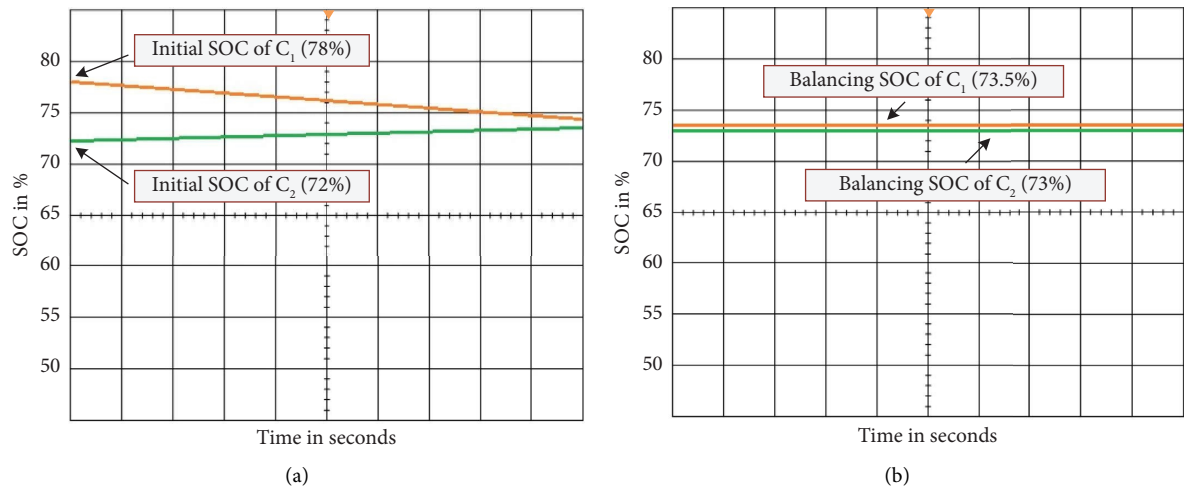

Figure 15: Real-time simulation results of cell 1 and cell 2. (a) Before balancing. (b) After balancing.

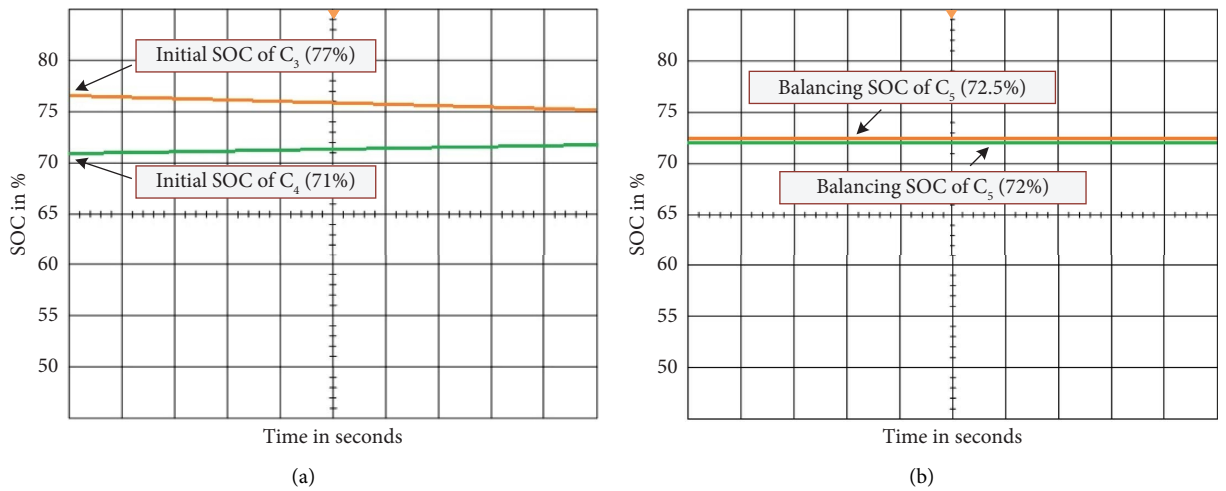

Figure 16: Real-time simulation results of cell 3 and cell 4. (a) Before balancing. (b) After balancing.

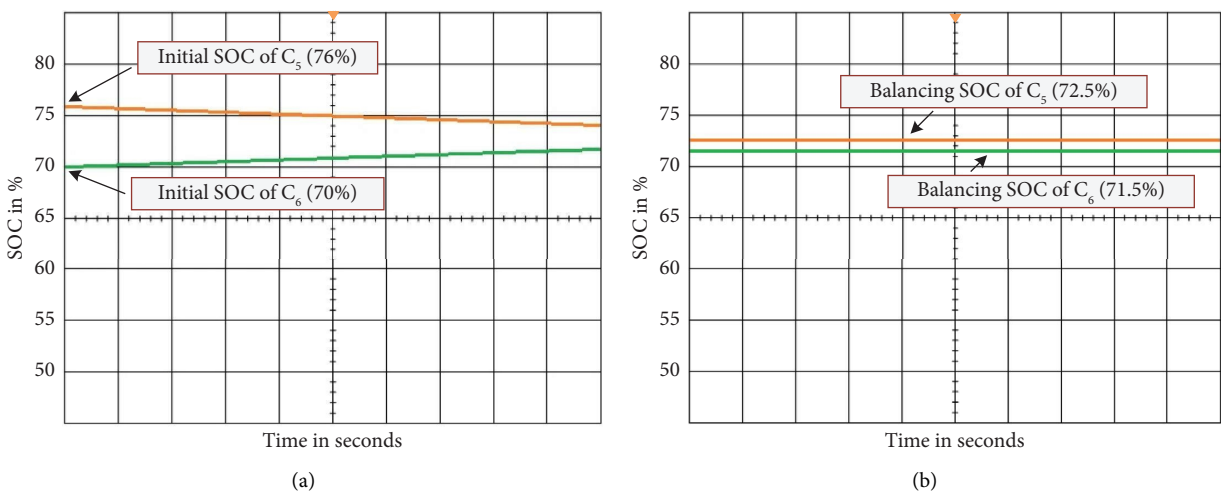

Figure 17: Real-time simulation results of cell 5 and cell 6. (a) Before balancing. (b) After balancing.

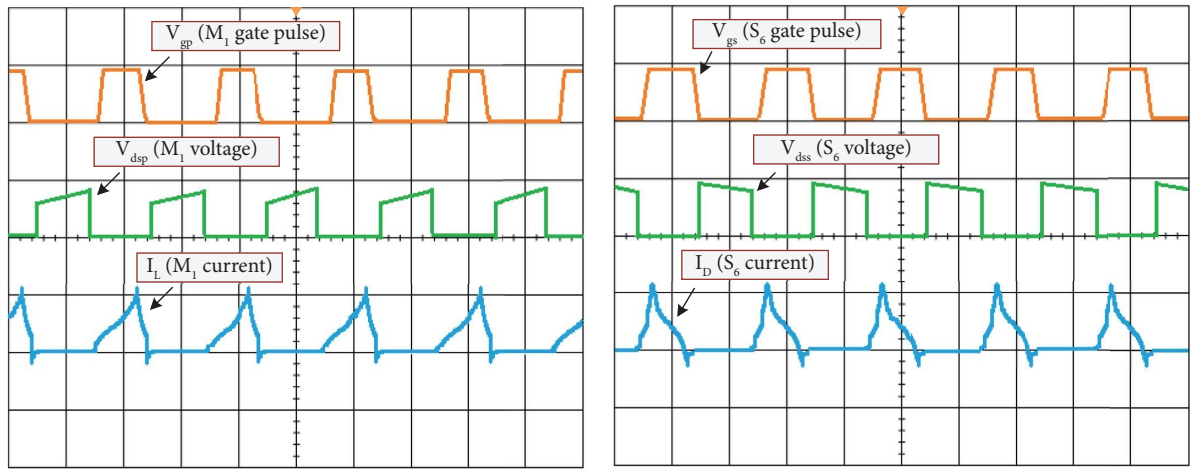

Figure 18: Real-time simulation switching waveform. (a) Mode 1. (b) Mode 2.

and 6 before balancing, while Figure 17(b) depicts the SOC of cells 5 and 6 after balancing. From the graph, it is clear that cell 5 gets balanced at SOC of 72.5% and cell 6 gets balanced at SOC of 71.5%, respectively.

The switching characteristics of various switches in the proposed topology are analysed through the real-time simulator. The switching waveform of the real-time simulator is illustrated in Figure 18. As per the balancing principle shown in Figure 5, the switches involved in mode 1 and mode 2 operations are considered. Switch M_1 takes part in mode 1 operation, and switch S_6 takes part in mode 2 operation. Cell C_6 is considered a weaker cell; hence, the battery pack energy is transferred to C_6 to achieve a balancing state. Figure 18(a) depicts the voltage and current of switch M_1 after it is activated by gate pulse V_{gp}. At the end of mode 1, the battery pack energy is charged in the inductor, and the charging current I_L flows through the switch M_1. Figure 18(b) depicts the voltage and current waveform of switch S_6 after it is turned on via gate pulse V_{gs}. At the end of mode 2, the inductor's stored energy is discharged to C_6, and the discharging current I_D travels through switch S_6.

From the abovementioned real-time simulator results, the balancing efficiency is calculated as

$$\eta_{b(\text{real-time})} = \frac{\sum_{i=1}^{n} \text{SOC}_{e_i}}{\sum_{i=1}^{n} \text{SOC}_{s_i}} \times 100\%, \tag{39}$$

where $\eta_{b(\text{real-time})}$ is the balancing efficiency of real-time simulation, SOC_{e_i} is the SOC at the end of balancing, SOC_{s_i} is the SOC at the start of balancing, and n denotes the number of cells. The balancing efficiency of real-time simulation is 97.75%, whereas the balancing efficiency of MATLAB simulation output (static mode is noted as 98.78%; hence, the deviation in balancing efficiency of 0.81%) was observed among real-time simulation and MATLAB simulation.

6. Conclusion

This paper proposes an improved bi-switch flyback converter with a single-input and multioutput topology for lithium-ion battery pack balancing. The SOC imbalances at static states such as some high and some low, one high and some low, and some high and one low SOC imbalances are considered for analysing energy transfer characteristics. For SOC estimation, the proposed topology employs the Coulomb counting method. The proposed converter's switching and conduction losses were analysed for energy efficiency. Using MATLAB simulation software, the balancing parameters of the proposed topology and the conventional topology were verified. The proposed topology has a 0.4%–0.7% higher balancing efficiency than the conventional topology. The proposed topology offers up to two times the balancing speed compared to conventional topology. By using the OPAL-RT (OP5700) real-time simulator, the simulation outcome of the proposed topology is finally validated. Between MATLAB simulation and real-time simulation, a 0.81% difference in balancing efficiency was observed. Consequently, based on the preceding observation, the balancing efficiency and balancing speed of the proposed topology were improved.

Nomenclature

Terms and Abbreviations

$LiCoO_2$: Lithium cobalt oxide
$LiPF_6$: Lithium hexafluorophosphate
$LiMn_2O_4$: Lithium manganese oxide
$LifePO_4$: Lithium-ion phosphate
NCM: Nickel cobalt manganese
NCA: Nickel cobalt aluminium
SoH: State of health

ICs: Integrated circuits
MOSFET: Metal-oxide semiconductor field-effect transistor
PWM: Pulse width modulation
SOC: State of charge
EV: Electric vehicle
BMS: Battery management system
MATLAB: Matrix laboratory
DSO: Digital storage oscilloscope
LAN: Local area network
CC: Coulomb counting
KF: Kalman filter
DCM: Discontinuous conduction mode
FPGA: Field-programmable gate array
HIL: Hardware in the loop

List of Symbols

V_{Lp}: Primary inductor voltage
D: Duty cycle
T_t: Total period
I_{Lp}: Primary inductor current
$I_{P,\mathrm{ave}}$: Average primary current
$I_{\mathrm{pp,ave}}$: Average primary peak current
L_p: Primary inductor
L_m: Magnetising inductance
$Q(t)$: Available battery capacity
Qn: Nominal battery capacity
$P_{R_{\mathrm{ss}}}$: Secondary switch resistive loss
P_{con}: Conduction loss
P_{ohmic}: Ohmic loss
P_{core}: Core loss
P_e: Eddy current loss
P_h: Hysteresis losses
B_m: Maximum flux density t lamination thickness
f_{sw}: Frequency
V: Core volume.

Data Availability

The results presented in this study are based on simulations. The underlying data used to support the findings of this study are available from the corresponding author upon request.

Conflicts of Interest

The authors declare that they have no conflicts of interest.

References

[1] S. W. Lee, K. M. Lee, Y. G. Choi, and B. Kang, "Modularized design of active charge equalizer for li-ion battery pack," *IEEE Transactions on Industrial Electronics*, vol. 65, no. 11, pp. 8697–8706, 2018.

[2] N. Ghaeminezhad, Q. Ouyang, X. Hu, G. Xu, and Z. Wang, "Active cell equalization topologies analysis for battery packs: a systematic review," *IEEE Transactions on Power Electronics*, vol. 36, no. 8, pp. 9119–9135, 2021.

[3] A. Dong, R. Ma, and Y. Deng, "Optimization on charging of the direct hybrid lithium-ion battery and supercapacitor for high power application through resistance balancing," *Energy*, vol. 273, 2023.

[4] S. Rana, R. Kumar, and R. S. Bharj, "Current trends, challenges, and prospects in material advances for improving the overall safety of lithium-ion battery pack," *Chemical Engineering Journal*, vol. 463, 2023.

[5] J. H. Ahn and B. K. Lee, "High-efficiency adaptive-current charging strategy for electric vehicles considering variation of internal resistance of lithium-ion battery," *IEEE Transactions on Power Electronics*, vol. 34, no. 4, pp. 3041–3052, 2019.

[6] J. V. Barreras, R. de Castro, Y. Wan, and T. Dragicevic, "A consensus algorithm for multi-objective battery balancing," *Energies*, vol. 14, no. 14, pp. 4279–4325, 2021.

[7] L. Hu, R. Hu, Z. Ma, and W. Jiang, "State of charge estimation and evaluation of lithium battery using kalman filter algorithms," *Materials*, vol. 15, no. 24, p. 8744, 2022.

[8] Z. Zhou, B. Duan, Y. Kang, N. Cui, Y. Shang, and C. Zhang, "A low-complexity state of charge estimation method for series-connected lithium-ion battery pack used in electric vehicles," *Journal of Power Sources*, vol. 441, 2019.

[9] X. Tang, Y. Zhou, F. Gao, and X. Lai, "Joint estimation of state-of-charge and state-of-health for all cells in the battery pack using "leader-follower" strategy," *eTransportation*, vol. 15, 2023.

[10] H. Zhang, X. Tong, L. Zhang, and H. Fu, "Fast state-of-charge balancing control strategies for battery energy storage systems to maximize capacity utilization," *Journal of Energy Storage*, vol. 57, 2023.

[11] Z. B. Omariba, L. Zhang, and D. Sun, "Review of battery cell balancing methodologies for optimizing battery pack performance in electric vehicles," *IEEE Access*, vol. 7, pp. 129335–129352, 2019.

[12] W. Kurpiel, P. Deja, B. Polnik et al., "Performance of passive and active balancing systems of lithium batteries in onerous mine environment," *Energies*, vol. 14, no. 22, p. 7624, 2021.

[13] V. B. Vulligaddala, S. Vernekar, S. Singamla et al., "A 7-cell, stackable, Li-ion monitoring and active/passive balancing IC with in-built cell balancing switches for electric and hybrid vehicles," *IEEE Transactions on Industrial Informatics*, vol. 16, no. 5, pp. 3335–3344, 2020.

[14] T. Duraisamy and D. Kaliyaperumal, "Machine learning-based optimal cell balancing mechanism for electric vehicle battery management system," *IEEE Access*, vol. 9, pp. 132846–132861, 2021.

[15] M. Uzair, G. Abbas, and S. Hosain, "Characteristics of battery management systems of electric vehicles with consideration of the active and passive cell balancing process," *World Electric Vehicle Journal*, vol. 12, no. 3, p. 120, 2021.

[16] S. Hemavathi, "Overview of cell balancing methods for Li-ion battery technology," *WILEY*, vol. 203, pp. 1–12, 2020.

[17] X. Zhang, G. Zhou, and S. Liu, "Switched-capacitor equalizers using hybrid balancing paths for series-connected energy storage cells," *Journal of Energy Storage*, vol. 63, 2023.

[18] Y. Li, J. Xu, X. Mei, and J. Wang, "A unitized multiwinding transformer-based equalization method for series-connected battery strings," *IEEE Transactions on Power Electronics*, vol. 34, no. 12, pp. 11981–11989, 2019.

[19] X. Qi, Y. Wang, and M. Fang, "An integrated cascade structure-based isolated bidirectional DC-DC converter for battery charge equalization," *IEEE Transactions on Power Electronics*, vol. 35, no. 11, pp. 12003–12021, 2020.

[20] T. E. Fan, S. M. Liu, H. Yang, P. H. Li, and B. Qu, "A fast active balancing strategy based on model predictive control for lithium-ion battery packs," *Energy*, vol. 279, 2023.

[21] Y. Li, P. Yin, and J. Chen, "Active equalization of lithium-ion battery based on reconfigurable topology," *Applied Sciences*, vol. 13, no. 2, p. 1154, 2023.

[22] S. Lee, M. Kim, J. W. Baek, D. W. Kang, and J. Jung, "Enhanced switching pattern to improve cell balancing performance in active cell balancing circuit using multi-winding transformer," *IEEE Access*, vol. 8, pp. 149544–149554, 2020.

[23] S. Chakraborty, H. N. Vu, M. M. Hasan, D. D. Tran, M. E. Baghdadi, and O. Hegazy, "DC-DC converter topologies for electric vehicles, plug-in hybrid electric vehicles and fast charging stations: state of the art and future trends," *Energies*, vol. 12, no. 8, p. 1569, 2019.

[24] W. Chen, Z. Ding, J. Liu, J. Kan, M. S. Nazir, and Y. Wang, "Half-bridge lithium-ion battery equalizer based on phase-shift strategy," *Sustainability*, vol. 15, no. 2, p. 1349, 2023.

[25] S G A P N and A. P. N, "An extended Kalman-Bucy filter for state of charge estimation of 2-RC network modelled Li-ion battery," *E-Prime-Advances in Electrical Engineering, Electronics and Energy*, vol. 6, 2023.

[26] A. Turksoy, A. Teke, and A. Alkaya, "A comprehensive overview of the dc-dc converter-based battery charge balancing methods in electric vehicles," *Renewable and Sustainable Energy Reviews*, vol. 133, 2020.

[27] X. Guo, J. Geng, Z. Liu, X. Xu, and W. Cao, "A flyback converter-based hybrid balancing method for series-connected battery pack in electric vehicles," *IEEE Transactions on Vehicular Technology*, vol. 70, no. 7, pp. 6626–6635, 2021.

[28] Y. Cao, K. Li, and M. Lu, "Balancing method based on flyback converter for series-connected cells," *IEEE Access*, vol. 9, pp. 52393–52403, 2021.

[29] U. J. Kim and S. J. Park, "New cell balancing technique using SIMO two-switch flyback converter with multi cells," *Energies*, vol. 15, no. 13, p. 4806, 2022.

[30] K. Soltanzadeh and M. R. Yousefi, "Analysis and design of two-switch flyback converter with double passive lossless snubber," *IET Power Electronics*, vol. 11, no. 7, pp. 1187–1194, 2018.

[31] A. L. Eshkevari, A. Mosallanejad, and M. Sepasian, "Design, modelling, and implementation of a modified double-switch flyback-forward converter for low power applications," *IET Power Electronics*, vol. 12, no. 4, pp. 739–748, 2019.

[32] W. Han, C. Zou, C. Zhou, and L. Zhang, "Estimation of cell SOC evolution and system performance in module-based battery charge equalization systems," *IEEE Transactions on Smart Grid*, vol. 10, no. 5, pp. 4717–4728, 2019.

[33] Y. Lin, X. Xu, F. Wang, and Q. Xu, "Active equalization control strategy of Li-ion battery based on state of charge estimation of an electrochemical-thermal coupling model," *International Journal of Energy Research*, vol. 44, no. 5, pp. 3778–3789, 2020.

[34] Z. Zhang, L. Zhang, L. Hu, and C. Huang, "Active cell balancing of lithium-ion battery pack based on average state of charge," *International Journal of Energy Research*, vol. 44, no. 4, pp. 2535–2548, 2020.

[35] G. Sugumaran and N. Amutha Prabha, "A comprehensive review of various topologies and control techniques for DC-DC converter-based lithium-ion battery charge equalization," *International Transactions on Electrical Energy Systems*, vol. 2023, Article ID 3648488, pp. 1–21, 2023.

[36] Y. Ye, J. Wang, and X. Wang, "A multi-winding transformer-based active cell equalizer with self-driven switches for series-connected lithium-ion batteries and super-capacitors," *Journal of Energy Storage*, vol. 70, 2023.

[37] Y. L. Lee, C. H. Lin, and S. J. Yang, "Power loss analysis and a control strategy of an active cell balancing system based on a bidirectional flyback converter," *Applied Sciences*, vol. 10, no. 12, p. 4380, 2020.

[38] Y. L. Lee, C. H. Lin, S. A. Farooqui, H. D. Liu, and J. Ahmad, "Validation of a balancing model based on master-slave battery management system architecture," *Electric Power Systems Research*, vol. 214, 2023.

[39] G. V. B. Kumar, P. Kaliannan, S. Padmanaban, J. B. Holm-Nielsen, and F. Blaabjerg, "Effective management system for solar PV using real-time data with hybrid energy storage system," *Applied Sciences*, vol. 10, no. 3, p. 1108, 2020.

[40] R. K. Sarojini, P. Kaliannan, Y. Teekaraman, S. Nikolovski, and H. R. Baghaee, "An enhanced emulated inertia control for grid-connected pv systems with hess in a weak grid," *Energies*, vol. 14, no. 6, p. 1721, 2021.